

Water motion relative to subtidal kelp fronds

C. L. Stevens¹

National Institute of Water and Atmospheric Research, Greta Point, P.O. Box 14-901 Kilbirnie, Wellington, New Zealand

C. L. Hurd

Department of Botany, University of Otago, P.O. Box 56, Dunedin, New Zealand

M. J. Smith

National Institute of Water and Atmospheric Research, Greta Point, P.O. Box 14-901 Kilbirnie, Wellington, New Zealand

Abstract

A study of water velocities near subtidal kelp fronds, relative to the motion of the kelp itself, is described. The dynamic model developed by Utter and Denny (1996) is used to develop a quantitative measure of the relative velocity vector, \bar{u}_r . The numerical model is extended through the addition of a current, use of a larger drag coefficient, and explicit consideration of \bar{u}_r . The model is tested by comparing it with microwave radar observations of a tethered float. The modeling of kelp frond motion uses parameters derived from current meter observations as input data. The results indicate that the relative velocity of seawater to the kelp frond is rarely zero and often is of comparable magnitude to the local Eulerian velocity of the water relative to the seabed. This has ramifications for modeling of both drag and boundary-layer transport processes. Use of a monochromatic wave field in the modeling in conjunction with examination of the results in the time domain suggests the magnitude of the current is very important in controlling motion at frequencies lower than the wave frequency.

Subtidal kelps such as *Macrocystis integrifolia*, *Macrocystis pyrifera*, and *Nereocystis luetkeana* are important components of the coastal communities of temperate zones of the Pacific coasts of the Americas and southern New Zealand (Lobban 1978; Kain 1982; Koehl and Alberte 1988; Hay 1990). They are characterized by a long stipe, enabling them to be anchored in relatively deep water, that connects the holdfast to the floating productive region where blades are buoyed at the water surface by air bladders (Lobban 1978; Kain 1982; Koehl and Alberte 1988). The rates of production of these kelp are influenced by the velocity of water at the blade surface.

There are two major research themes associated with boundary layers around subtidal kelp fronds. First, the ability to withstand the forces imparted by waves that stretch and move the fronds is crucial for macroalgal survival in wave-swept environments (Koehl and Alberte 1988; Denny et al. 1998). Second, the boundary layers that develop with flow past the fronds influence the rates of nutrient transport to the algae (Hurd et al. 1996; Hurd 2000). A fundamental quantity for both themes is the velocity of water outside the blades'

boundary layer ("local water") relative to the frond, termed the relative velocity \bar{u}_r (the overbar denotes a vector quantity). This is the vector difference between the motion of the water, $\bar{u}_w + u_c$ (wave velocity \bar{u}_w plus horizontal current u_c ; in this two-dimensional representation, u_c has no overbar), and the velocity of the kelp frond itself, \bar{u}_k , in a frame of reference fixed relative to the bed (see Fig. 1a). While $\bar{u}_w + u_c$ is readily measured, accurate determination of \bar{u}_r is critical for our understanding of how kelps interact with waves and currents.

Technical difficulties associated with measuring velocities adjacent to kelp blade surfaces (but outside the kelp blade's boundary layer) mean that there are presently no direct measurements of \bar{u}_r for kelps. For example, to measure \bar{u}_r in the field requires instruments that are waterproof and can survive wave impact and contact with neighboring algae. The velocity should be recorded outside the blade's boundary layer and should be achieved in such a way as not to affect the algal strength, flexibility, or buoyancy. Finally, the magnitude of the velocity measurements may be quite small (Seymour 1996), perhaps only a few centimeters per second. At the time of writing, there are no instruments able to provide a measure of \bar{u}_r . Consequently, numerical modeling, combined with direct measurements of seawater velocities, is the most useful tool available for determining \bar{u}_r .

In the past, two approaches have been taken to describe \bar{u}_r . In one scenario, the frond moves passively with the fluid, and \bar{u}_r is zero (Seymour 1996). Analysis of tethered floats has been used to justify this approximation (Seymour 1996), but the analysis focused on the orbital movement of waves and did not include a current flowing in addition to waves. Because the drag force, as well as other forces, typically acts in a nonlinear fashion, the added effect of a current cannot be linearly added to the existing effects of the wave motion.

¹ Corresponding author (c.stevens@niwa.cri.nz).

Acknowledgments

The authors thank Gregory Lawrence, Paul J. Harrison, Stephen Pond, Andrew Spencer, Pål Isachsen, John McGregor, Murray Poulter, Christopher Hepburn, and John Boom for encouragement and support. Conrad Pilditch generously provided access to his seawater flume at the University of Waikato. Deane Harder and two anonymous reviewers are thanked for useful comments on the paper. The work was made possible by the New Zealand Royal Society Marsden Fund, the New Zealand Foundation for Research Science and Technology, the Canadian Natural Science and Engineering Research Council, and Bamfield Marine Station.

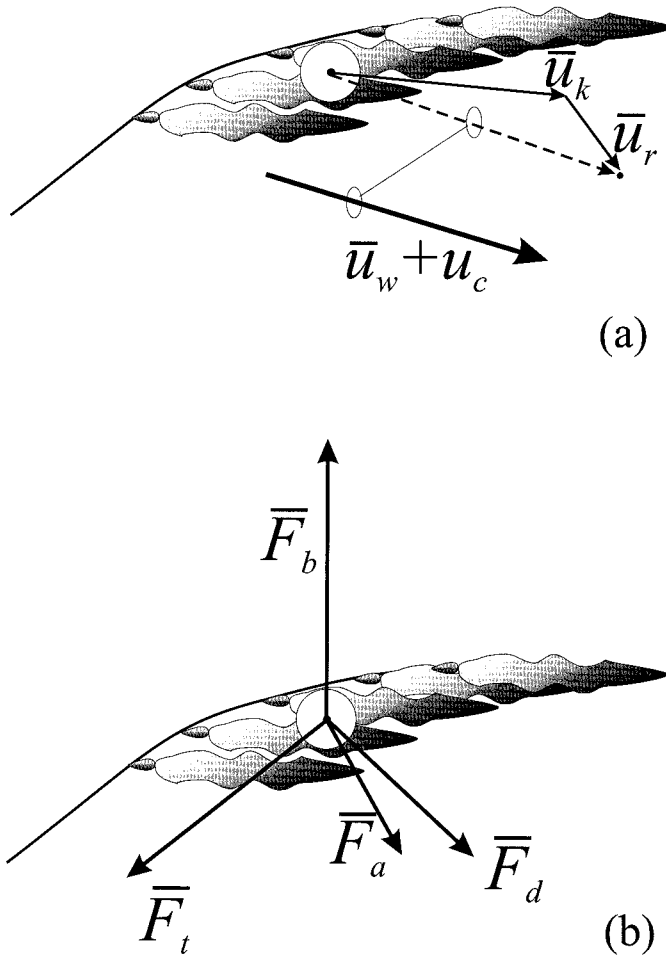


Fig. 1. Stylized *Macrocystis* frond with the position of the centroid indicated by a hollow circle. (a) Velocity vector diagram. The relative velocity \bar{u}_r is the vector difference between the velocity of the water outside the frond boundary-layer \bar{u}_w and the velocity of the kelp frond \bar{u}_k (see text for further details). (b) Free-body diagram showing the force vectors (buoyancy \bar{F}_b , drag \bar{F}_d , added mass reaction \bar{F}_a , and tension \bar{F}_t) acting on the idealized kelp frond mass.

In the natural situation, Stokes drift alone will ensure that there is some mean current whenever there are waves, and measurements clearly show that an average current due to wind or alongshore drift is often present in addition to waves (Stevens and Hurd 1997; Jackson 1998). In the alternate scenario, the frond has been considered rigid, so measurements in a Eulerian frame, as resolved with a fixed current meter (Jackson and Winant 1983; Stevens and Hurd 1997), are appropriate. The Eulerian frame is an approximation, as fronds are commonly observed to sway and move in the flow. The natural situation will lie within these two extreme bounds.

The overall objective of this study was to quantify the likely relative velocities of kelp fronds that are influenced by both surface waves and unidirectional currents. Our starting point was to use the model of Utter and Denny 1996, hereinafter “UD96,” to resolve \bar{u}_r . We extended the model of UD96 by adding a background current to the wave field and incorporated an improved drag coefficient obtained from

flume measurements at speeds likely to be encountered by subtidal kelps in the field. To test the model, we compared it to radar observations of tethered floats, previously used as a proxy for kelp frond motion (Seymour 1996). Finally, we used parameters derived from measurements of seawater velocities adjacent to a *Macrocystis* sp. bed in a Eulerian reference frame to drive the model.

Materials and methods

A force-balance model for the frond—The relative velocity \bar{u}_r is derived from analytic expressions for \bar{u}_w and numerical computations of \bar{u}_k , where \bar{u}_k is calculated from the force balance of the frond, described in UD96. Using the notation of UD96, the acceleration of a body (i.e., a kelp frond), \bar{a}_k , is given by

$$\bar{a}_k = \frac{\bar{F}_b + \bar{F}_d + \bar{F}_a + \bar{F}_t}{M_e} \quad (1)$$

where the vector forces are buoyancy \bar{F}_b , drag \bar{F}_d , added mass reaction \bar{F}_a , and tension \bar{F}_t , acting on an effective mass, M_e (i.e., that which is adjusted for the added mass effect; Denny 1988). As illustrated in Fig. 1b, the buoyancy force \bar{F}_b acts vertically, \bar{F}_d acts in the direction of local relative flow, \bar{F}_a acts mainly in the direction of local water acceleration, and \bar{F}_t acts in the direction of the stipe but only when it is fully elongated. The effective mass is given by $M_e = M + \rho_w C_a V$, where ρ_w is water density ($1,025 \text{ kg m}^{-3}$), M is the frond mass, C_a is the added mass coefficient, and V is frond volume.

The most important extension from the model described by UD96 is the addition of a horizontal mean current, u_c , aligned with the waves, which affects a number of the force components as well as the apparent frequency of the wave field. The wave velocity \bar{u}_w is the vector sum of u and v , the horizontal and vertical velocity component fields under the waves (Fig. 2a). Hence, the local absolute velocity at any point is a summation of u_c (horizontal only) and the wave components u and v (Fig. 2b).

The model considers a monochromatic wave field of peak-to-peak height H (see Fig. 2a); angular frequency $\omega = 2\pi/T$, where T is the wave period; and the radian wavenumber $k = 2\pi/\lambda$, where λ is the wavelength. The coordinate system origin is located at the mean water surface, directly above the holdfast (located at the seabed at $y = -d$, where the water depth = d); x is positive in the direction of the waves and current, and the vertical coordinate y is negative pointing downwards. The wave velocity components are given by

$$u = \frac{H\omega}{2} \cos(kx - \omega t) \frac{\cosh(k(y + d))}{\sinh(kd)} \quad \text{and} \quad (2)$$

$$v = \frac{H\omega}{2} \sin(kx - \omega t) \frac{\sinh(k(y + d))}{\sinh(kd)} \quad (3)$$

The components of fluid acceleration \bar{a}_w can be obtained from differentiation of u and v with respect to time. In the presence of a current, the apparent frequency recorded by a stationary observer is modified as $\omega' = \omega/(1 - u_c/c_p)$, where c_p is the phase velocity $c_p = \omega/k$ (Dean and Dalrymple

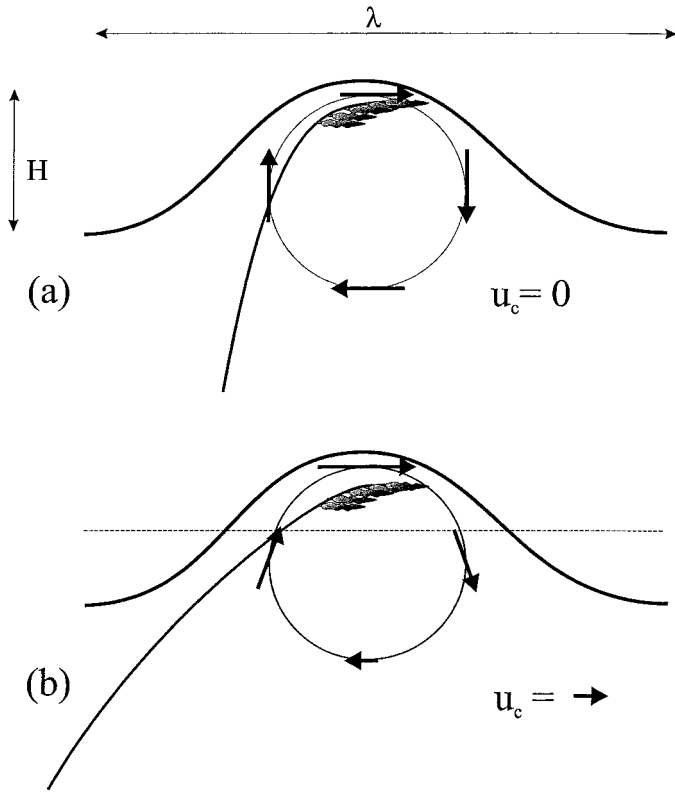


Fig. 2. Sketches of a kelp frond in an orbital wave field, with waves of wavelength λ and height H . In (a), there is no current, and the horizontal (u) and vertical (v) vector components are of a similar magnitude. In (b), a cross-flow current u_c is added to the wave field. The local velocity is a summation of u_c and the wave components u and v .

1984). Hence, the frequency in Eq. 2 and 3 is replaced with ω' . The wavenumber viewed by the observer is unchanged. The buoyancy force is given by

$$\bar{F}_b = \bar{g}V(\rho_k - \rho_w) \quad (4)$$

where \bar{g} is the acceleration due to gravity (9.8 m s^{-2} in the downwards direction). The frond density, ρ_k , is lighter than water and was determined here by measuring the force required to submerge *Macrocystis* blades of a known volume. This value will vary depending on the size of each blade and pneumatocyst, but for the *Macrocystis* blades used in our drag experiments (see later), ρ_k was around 985 kg m^{-3} . In the kelp frond example used in the initial numerical model, the buoyancy force was $\sim 2 \text{ N}$ and is comparable to UD96, which used $|\bar{F}_b| = 2.5 \text{ N}$. Following Denny et al. (1997), \bar{F}_b changes sign when the frond crosses the water surface, and a smoothing is applied based on a lengthscale of the square root of the projected area. This significantly reduces unrealistic accelerations and forces observed in the model simulations in the absence of this smoothing. The frond volume V was calculated by multiplying the projected frond surface area, normal to the direction of flow, by the blade thickness.

The drag force requires knowledge of \bar{u}_r , so that

$$\bar{F}_d = \frac{1}{2}\rho_w \bar{u}_r^\gamma A S_d \quad (5)$$

where S_d is a shape factor, γ is an empirical power law coefficient, and A is the projected area of the frond when looking at the blades normal to the flow. For example, a frond might possess 10 blades, each 0.5 m long and 0.1 m wide. UD96 (and Denny et al. 1997) indicates that $\gamma = 1.6$ and $S_d = 0.016$ where their shape factor S_d was derived from experiments in which velocities were $> 0.5 \text{ m s}^{-1}$. If the present model uses this value for S_d , the tethered body experiences very little drag at all. So much so that, in preliminary simulations using the kelp parameters described later, the frond was hardly influenced by the flow. We supposed that S_d was underestimated at the lower velocities ($< 0.5 \text{ m s}^{-1}$) that are commonly observed in *Macrocystis* beds (Stevens and Hurd 1997; Jackson 1998). Gaylord et al. (1994) and Gaylord (2000) note that S_d increases significantly at lower flow rates. In the next section, we describe experiments to improve drag parameterization at low flows ($< 0.5 \text{ m s}^{-1}$). This was achieved by using a classical drag coefficient approach whereby Eq. 5 is cast in terms of u^2 so that our drag coefficient is $C_d = u^{(\gamma-2)} S_d$. This approach was chosen because we consider that the mechanistic scaling $F_d \sim u^2$ should hold and that systematic variability is related to changes in boundary-layer structure and effective frond area.

The added mass reaction force uses the derived acceleration of the kelp frond relative to the local water, \bar{a}_r . This is calculated using the difference between that derived from the change in frond position and the analytic value for \bar{a}_w , so that

$$\bar{F}_a = \rho_w C_a V \bar{a}_r + \rho_w V \bar{a}_w,$$

where C_a is set to 2.0 (Gaylord et al. 1994; see Discussion).

The tension along the stipe of unstretched length l_0 is assumed to be zero if $(x^2 + (d + y)^2)^{1/2} < l_0$; otherwise,

$$\bar{F}_t = C_t A_{xs} \left(\frac{(x^2 + (d + y)^2)^{1/2} - l_0}{l_0} \right)^\alpha.$$

This requires knowledge of the stipe cross-sectional area A_{xs} and two elasticity-based empirical coefficients, the coefficient of tension C_t and α , which for some kelps have been measured as $C_t = 1.9 \times 10^7$ and $\alpha = 1.41$ (UD96). Here, A_{xs} is determined from direct measurements of stipe width using calipers, which is set at 5 mm . The force balance is solved for \bar{a}_k , then \bar{u}_k is calculated by numerical integration. From this calculation, \bar{u}_r may be derived using the vector addition shown in Fig. 1a, as \bar{u}_w is known everywhere within the fluid domain. Explicit time stepping was used with a time step $\sim 0.01 \text{ s}$. Most experiments were run for at least 200 s of model time to allow a steady state to develop.

In considering kelp survivorship, Méndez et al. (1999) and UD96 used continuous wave distributions as forcing for their modeling, which allowed the development of a statistical appreciation of the results. Here, we use a monochromatic wave, as this simplifies interpretation and enables identification of where, within the wave phase, the enhanced relative motion occurs. A summary of parameters that vary between the float and kelp model scenarios used in the Results section is given in Table 1.

Table 1. Values used for the basic model parameters for the float and kelp scenarios, with symbols and units in parentheses.

	Float	Kelp
Current u_c (m s^{-1})	0.2	0.05
Tension coefficient C_t	2×10^8	1.9×10^7
Stipe length l_0 (m)	5	12
Wavelength λ (μ)	10.8	51
Wave period T (s)	2.8	7
Wave height H (m)	0.7	0.25
Water depth (m)	2	6
Object density ρ_k (kg m^{-3})	225	985
Volume V (m^3)	8×10^{-3}	5×10^{-3}

To illustrate the model force components, Fig. 3 plots a subset of the numerical force vectors for a segment of the kelp simulation. The force components (\bar{F}_b , \bar{F}_d , \bar{F}_a , and \bar{F}_t) are shown in offset vector arrows along with traces of the water elevation and the location of the kelp blade. The buoyancy \bar{F}_b acts variably as it is near the surface, and the occasional large spikes are when the frond rises above the water surface, changing the direction of the buoyancy force. For these particular parameters, this directional change happens with every wave. \bar{F}_d clearly shows the effect of the frond being pulled through the crest. The \bar{F}_a is typically

around the same magnitude as \bar{F}_d but is related to the rapid accelerations when the frond goes through the water surface (see Discussion). \bar{F}_t acts only at the crests of the waves for a short period, and, interestingly, this does not occur on every wave. The tension from a previous wave is sufficient to pull the frond far enough forward that it takes two waves to re-tension the frond (see Denny et al. 1997). Finally, \bar{u}_r peaks around the wave crest, and note that there is still a moderate \bar{u}_r when the stipe is not re-tensioned.

Laboratory estimates of drag forces on Macrocyctis fronds—Drag coefficients were directly measured using a variety of individual *M. pyrifera* blades, 3-m-long fronds, and pairs of fronds. The experiments were conducted at outer velocities that macroalgae are likely to encounter in the field (Stevens and Hurd 1997; Jackson 1998). *M. pyrifera* fronds with morphologies typical of those found exposed to waves and currents were collected from Harrington Point and Wellers Rock, Otago, New Zealand, and transported on ice to the University of Waikato, Hamilton, New Zealand. Selected frond sections were placed in a recirculating seawater flume (7 m long and 0.5 m wide, with water depths of ~ 0.3 m) operating at five velocities between 0.05 and 0.6 m s^{-1} (flume design based on Muschenheim et al. 1986). A SONTEK acoustic Doppler velocity turbulence probe was used

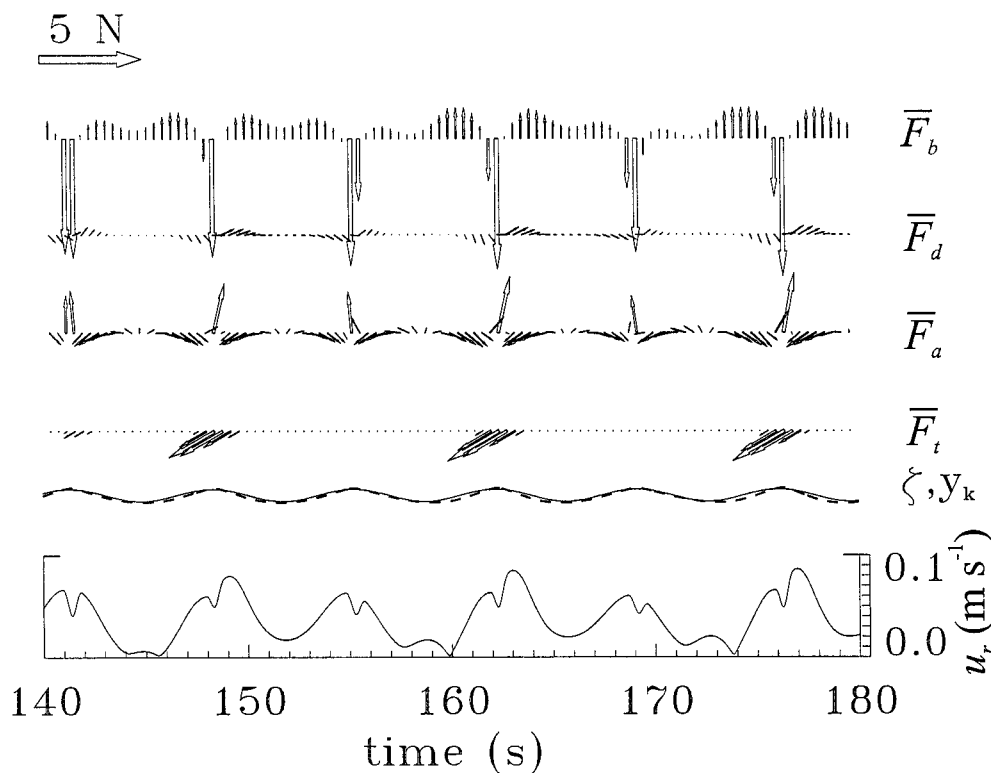


Fig. 3. Model results for force vectors in N (buoyancy \bar{F}_b , drag \bar{F}_d , added mass reaction \bar{F}_a , and tension \bar{F}_t) for the kelp scenario. \bar{F}_b , \bar{F}_d , \bar{F}_a , and \bar{F}_t are each offset vertically and identified on the right-hand side. The bottom axis represents time, so that the base of each force vector arrow denotes the time at which the force vector occurred. The lowest trace on the plot (with its axis on the lower right-hand side) shows the magnitude of \bar{u}_r , and directly above this trace is a time series of the water-surface elevation ζ (solid line) and the frond location y_k (dashed line). Note that every 40th calculation is shown. A scale vector is marked.

to calibrate the flume and detect steady-state flows following flume speed changes. A miniature load cell (GS Sensors, XFTC-101, ± 2 N cell) suspended on a vertical rod at a point just above the water was attached to the frond using a 2-m nylon line. The load cell axis was oriented near to the angle of the nylon line, and as the fronds floated at the surface for most of the experimental runs, the angle was never > 10 degrees, so the error resulting from the angle being offset from zero was minimal.

A variety of parameters, including the static projected area of the frond, were recorded (see Hurd et al. 1996). However, it was also necessary to use digital video to estimate the in situ projected area, because the fronds would compress and intertwine due to the drag effects (see fig. 7 in Hurd and Stevens 1997). The calibrated voltage output from the load cell was recorded on a Tektronics digital oscilloscope and averaged over several seconds. This device has a variable input gain providing high resolution, and drag could be measured for single kelp blades at flume flow rates as low as 0.05 m s^{-1} .

To validate our measurements of drag coefficients on kelp blades and fronds, we also estimated drag coefficients of spheres, as their drag coefficients are well described in the literature (Denny 1988). Drag coefficients of ping-pong balls (diameter = 3.75 cm) were measured, although this proved difficult at velocities below 0.25 m s^{-1} , as they were not perfectly neutrally buoyant and thus the spheres would encounter the water surface and the flume bed.

Remote sensing and field measurements—Seymour (1996) considered the analogy of a tethered float with an analytic model and then stated that the addition of a current would result in deviations from $\bar{u}_r = 0$. Measuring float velocity in situ has many of the same difficulties as measuring kelp frond motion. However, remote sensing using a dual-polarized microwave radar (for details, see Poulter et al. 1995) allows the accurate determination of float and neighboring wave velocities. The radar thus allowed us to compare direct measurements of float velocities with the model of the float, thereby evaluating the behavior of our model.

The radar operates by transmitting a coded microwave waveform and measuring the signal reflected back from the water surface. This provides two types of information: (1) the strength of the reflected or backscattered power, which relates to how rough the surface is; and (2) the velocity of these reflecting features. This information is provided at a sequence of cells spaced 1.3 m along the pointing direction of the radar, with a typical lateral size of 20 m. The data cells are obtained throughout a region extending from 20 to 150 m away from the observer (Poulter et al. 1995). In addition, the radar can operate in two modes that are sensitive to different types of reflecting features. In vertical polarization mode (denoted VV), the dominant source of scatter is small-scale, resonant waves (~ 5 -cm length), which are advected in an oscillatory manner by the underlying orbital motion of the dominant ocean waves. As a consequence, the velocity of the VV-mode data is the wave orbital motion combined with any current (plus a known fixed contribution of the small-scale Bragg scattering waves; see Rees 1990). The wave height, period, and wavelength can be obtained

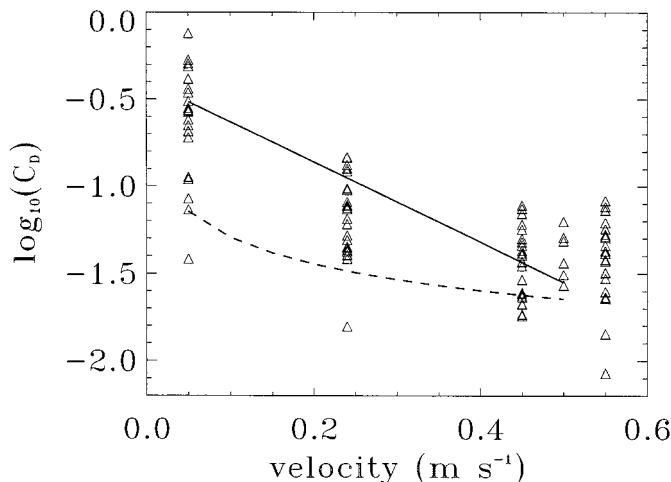


Fig. 4. Drag forces on *Macrocyctis* blades and fronds measured as a function of unidirectional flow speed. Results show calculated C_d as a function of unidirectional flow speed. Also included are the high-speed C_d value derived from the constant S_d used by UD96 as a dashed line and the model we have chosen to represent drag behavior (solid line).

from this information. In horizontally polarized mode (HH), the dominant source of backscatter is breaking wave plumes and any objects floating on the water surface (such as floats), with a velocity corresponding to those features.

The radar was mounted on an 8-m-high platform in the downwind shallows of the 15-km-wide Manukau Harbor, an estuary near Auckland, New Zealand, during November 1996. The water was ~ 2.5 m deep throughout the observation area. Four floats were deployed: one at 53 m, two at 58 m, and one at 63 m from the radar. The floats at 58 m were 20-cm-diameter polystyrene balls, while those at 53 and 63 m were of a similar size but shaped like cotton reels. The floats were tethered on 5-m-long polypropylene lines (4-mm diameter) to ballast blocks.

Current measurements next to a *Macrocyctis* bed at Dixon Island, Bamfield, British Columbia, Canada, were used to drive the kelp model. The measurements were made using an Interocceans S4 current meter (see Stevens and Hurd 1997 for details). Eighty velocity measurements were collected over a 2-min period, each hour, for 12 d during March 1994.

Results

Drag forces on Macrocyctis fronds—The drag coefficients obtained in flume experiments for the tethered spheres were lower than for a fixed sphere (e.g., Denny 1988) by a factor of 2. This was expected, as the tethered spheres were able to interact with their own wake. For the kelp blades and fronds, at the upper end of the velocity regime, the drag coefficient based on projected area matched the order of the UD96 work. However, the drag coefficient increased with decreasing velocity, so that at 0.05 m s^{-1} , it was ~ 0.5 . Figure 4 plots the results, including a line showing the high-speed $C_d = u^{(\gamma-2)}S_d$ used by UD96 (dashed). These experiments suggest that $C_d = 10^{(-2.3u-0.4)}$ (where u is measured in m s^{-1} , and γ is set to 2 rather than retained as a fitting parameter)

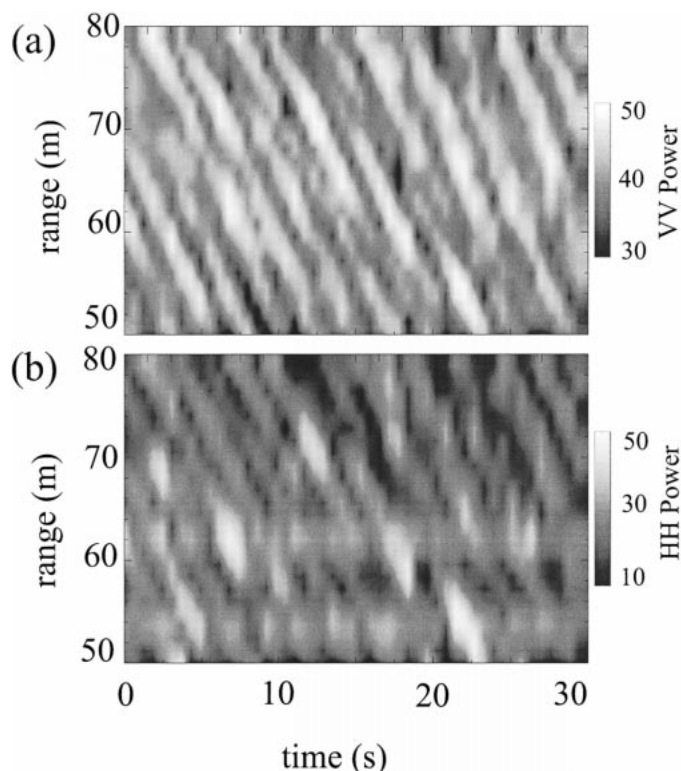


Fig. 5. Data images from the dual-polarized microwave radar. Backscatter of vertically polarized microwave (VV mode) is shown in (a) and horizontally polarized microwave (HH mode) in (b). The ocean waves manifest themselves as diagonal lines, and the floats are seen in (b) as blurred bright horizontal regions at 53 and 63 m (see Fig. 6 for an interpretive sketch).

is appropriate but for only for speeds $\leq 0.5 \text{ m s}^{-1}$ (Fig. 4, solid line). A linear fit to the exponent was used to approximate the data and minimize the calculation at each time step. The parameterization does not warrant enhanced detail, as issues related to frond compression and blade reorientation are not fully understood. In our kelp frond modeling, this parameter was applied in a dynamic fashion at every time step using \bar{u}_r as the velocity scale.

Observations and modeling of float velocity—Figure 5 shows simultaneous backscatter power images from (1) VV mode, which captures the wave field; and (2) HH mode, in which the floats are manifest. The VV image shows diagonal bands corresponding to wave crests approaching the observer, which are caused by enhanced backscatter near the wave crests. Spectral analysis of the time-space information indicates that the dominant period is $\sim 2.8 \text{ s}$ with a wavelength of 10 m. The HH-mode data are more complicated, and the interpretive sketch of Fig. 6 shows the wave crests approaching, along with the occasional large backscatter event from breaking waves and also the two quasicontinuous power bands due to the floats. The HH power shows some of the same information as the VV but is dominated by floats at two ranges, 53 and 63 m. The float power at 58 m is much weaker because the cotton reels used at 53 and 63 m provided a much better return signal. Note that float power ex-

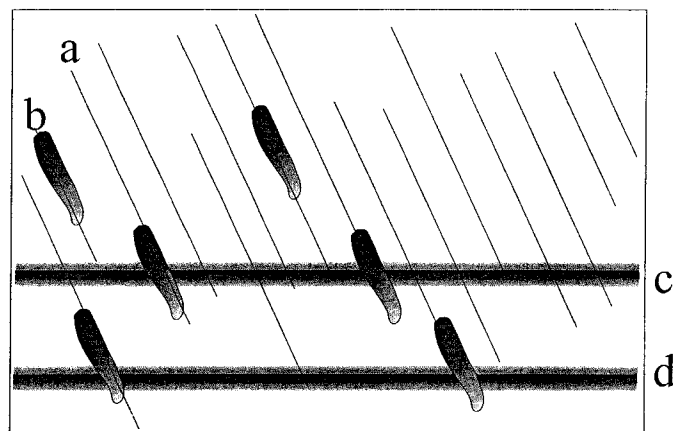


Fig. 6. An interpretive sketch of the HH-mode image from Fig. 5b. Marked are (a) the crests of the waves approaching the observer, (b) breaking wave events, and (c) and (d) the two bands of power associated with the tethered floats.

tends into adjacent range cells, due to the movement of the floats from one cell to the next and also slight smearing in the radar data processing.

The radar velocities are best considered using time-integrated ($> 2 \text{ min}$) distributions of velocity weighted by backscattered power from two individual range cells, one clear of the floats (75 m) and one containing a float (63 m). This yields Fig. 7, where negative velocities represent flow toward the observer; the solid line is from the range cell containing a float, and the dashed line is from the range without a float. The VV data (Fig. 7a) show that the distributions of wave velocity from the two ranges are almost identical, which is to be expected for a surface wind-drift current. As is typical, the VV distribution has a broader negative shoulder due to breaking wave plume backscatter and electromagnetic shadowing (Stevens et al. 1999). The VV peak at around -0.5 m s^{-1} identifies a current component toward the observer. After removal of the intrinsic speed of the ripples used for the radar Bragg backscatter (-0.3 m s^{-1}), the result is a -0.2 m s^{-1} current component. The HH data (Fig. 7b) at the two ranges are biased toward much more negative velocities than the VV data, with peaks at around -1.9 and -2.2 m s^{-1} for nonfloat and float, respectively. The distribution shown in Fig. 7b is typical of breaking wave plumes (Smith et al. 1996).

It is clear that the float-generated HH backscatter (Fig. 7b, solid line) contributes substantially to the high-velocity breaking data (velocities less than -1.6 m s^{-1} in Fig. 7b). It also generates a range of power close to zero velocity (Fig. 7b, shaded region). The contribution of backscatter at high velocities arises from the float as it is swept forward by the high-velocity wave crest, which is similar to backscatter from breaking wave plumes. The smaller local peak in Fig. 7b at -2.7 m s^{-1} is an instrument effect, as it occurs at all ranges. The local peak in the HH-float data at a velocity of -0.3 m s^{-1} is comparable to the current derived from the VV peak (-0.2 m s^{-1}). This arises during periods of no tension when the current moves the float toward the radar. All the power at more positive velocities (Fig. 7b, shaded

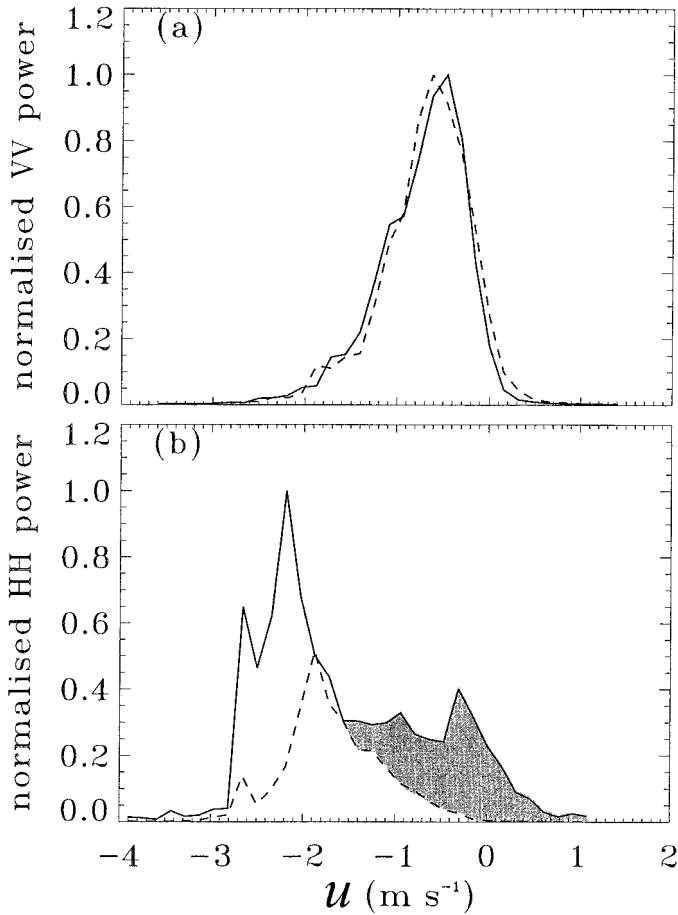


Fig. 7. Velocity distributions of Doppler-shifted radar backscatter showing data from two ranges, one with a float (solid lines) and the other without a float (dashed lines). Panel (a) shows the VV-mode orbital motions, while (b) shows the HH-mode equivalent data. The shaded region is related to the period when the float reaches the end of its tether and is dragged back into the wave (see text for details).

region) represents the float being pulled away from the observer as it rises over waves. This motion was also apparent from concurrent video recordings. If $\bar{u}_r = 0$, one would expect this part of the spectrum to match the VV because the float would exactly follow the waves. This is clearly not the case, and velocities in this region represent a significant departure from $\bar{u}_r = 0$.

The model simulation of the position of a float is shown in Fig. 8. This was achieved using appropriate parameters derived from the above data for wave height and period (H and T). Here, the current is $u_c = 0.2 \text{ m s}^{-1}$, and the peak oscillating velocity and period from the radar of $\sim 0.8 \text{ m s}^{-1}$ and 2.8 s , respectively, imply an $H \approx 0.7 \text{ m}$. Figure 8 is a side-view trace of the path of a body representing a tethered float under the influence of the modeled forces alone, as it is released from an arbitrary point beneath the water surface and downstream of the holdfast. The initial motion is mainly a combination of \bar{F}_d moving the body to the right and buoyancy moving the body rapidly upwards. Once the body reaches the surface, it floats and moves to the right until the

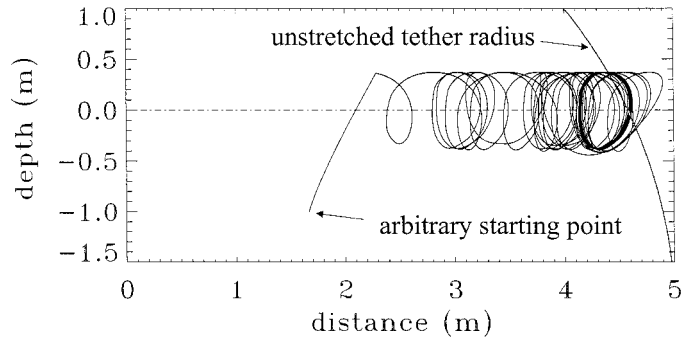


Fig. 8. A side view of the path followed by a tethered float as it is released from an arbitrary depth into wave field plus a current that is moving from left to right. The plot denotes the location of the float over time. The still-water surface is shown as a dotted horizontal line, and a radius showing the extent of the untensioned tether is indicated on the right-hand side.

tension on the stipe restrains it. The wave orbital motion interacts with the current to generate a looped trajectory that eventually stretches the stipe beyond its untensioned length. The buoyancy results in the float spending all time at or very near the water surface.

Figure 9a shows a time series of the velocity magnitudes $|\bar{u}_k|$, $|\bar{u}_w + u_c|$, and $|\bar{u}_r|$ from the steady-state period after the float has reached the end of its tether. The relative motion \bar{u}_r is always nonzero. The float follows the water motion for the rising velocity phase until just prior to the crest, at which time the tether begins to enhance $|\bar{u}_r|$, which is substantial until the trough is again reached. There is some modulation whereby the timescales of wave and kelp motion appear to be not exactly in phase, so that there is a kink in the $|\bar{u}_r|$ curve near the trough. Considering the horizontal component of \bar{u}_k (Fig. 9b), which would be measured by the radar, it is

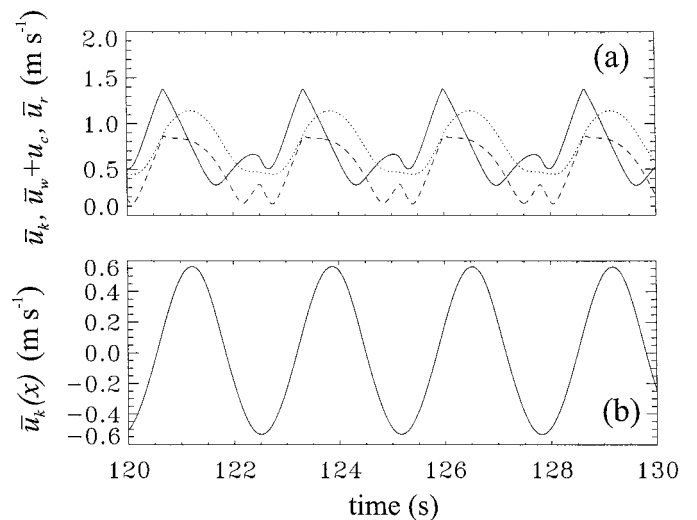


Fig. 9. A segment of model results for the tethered float observations. (a) Velocity magnitude time series for the kelp frond $|\bar{u}_k|$ (solid), water $|\bar{u}_w + u_c|$ (dotted), and relative velocity $|\bar{u}_r|$ (dashed). Note that these magnitude plots do not differentiate between flows in different directions. (b) The horizontal component (x) of \bar{u}_k .

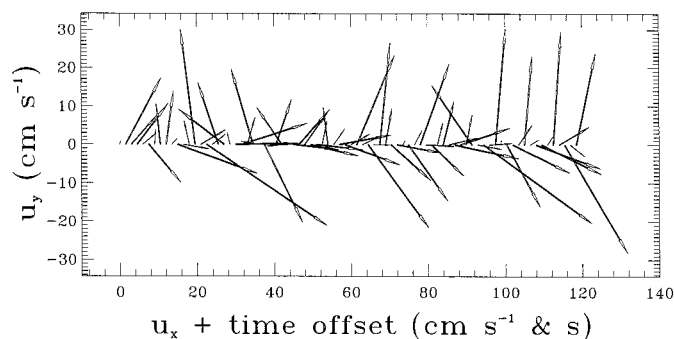


Fig. 10. Seawater velocities from a current-dominated site at Dixon Island, British Columbia. The velocity vectors are in the horizontal plane. The horizontal axis refers to the offset velocity magnitude (u) in direction x and also the time of the starting point of each vector (time offset).

apparent that this repeatedly changes sign and reaches absolute velocities of $\sim 0.5 \text{ m s}^{-1}$. This is comparable in magnitude with the half-width of the segment of the spectrum in Fig. 7b (shaded region) attributed to the floats and suggests that the tethered mass force-balance approach is suitable for analyzing the dynamics of this particular situation. It was these velocities directed away from the observer in the radar data that initially indicated the possibilities for the present application. In its present form, the model does not include the wave breaking.

Observations and modeling of a kelp frond—Figure 10 shows current vectors from a previously unpublished segment of the Hurd and Stevens (1997) data. These are horizontal velocities, so the viewpoint is from above. Consequently, these vectors are not directly analogous to the data in the vertical plane used in the modeling presented in this paper. The mean velocity is $u_c = 0.05 \text{ m s}^{-1}$, and the oscillating velocity is $\sim 0.15 \text{ m s}^{-1}$. The total water depth is 6 m, and the dominant wave period is $\sim 7 \text{ s}$. The velocities that result from depth correction of the S4 data (UD96) indicate an estimated wave height of 0.25 m from linear wave theory scaling where $H \sim |u_w|T/\pi$ and where $|u_w|$ is the maximum magnitude of the wave orbital velocity.

Simulation using these wave parameters results in the initial path shown in Fig. 11, which is equivalent to Fig. 8 but now for the body representing a kelp frond. The wavelength used in the float experiment (Fig. 8) is shorter ($\lambda = 11 \text{ m}$) than in the kelp experiment ($\lambda = 51 \text{ m}$). The stretched distances for the more elastic kelp stipe are comparable to that for the polypropylene, which is related to the small amplitude of the waves and current in the kelp scenario. Also, the u_c relative to the orbital speed is now increased, so the trajectory is less looped in the initial phase. Furthermore, the kelp body seems to find no single equilibrium path, in contrast with the float scenario. Instead, it has two preferred paths because, for most of the time, it takes two wave cycles to re-tension the stipe after a crest has been encountered (*see* Discussion).

Similar to Fig. 9a, a section of time series of model results for the velocity magnitude $|\bar{u}_r|$ are plotted in Fig. 12, along with concurrent $|\bar{u}_k|$ and $|\bar{u}_w + \bar{u}_c|$. In this simulation, the

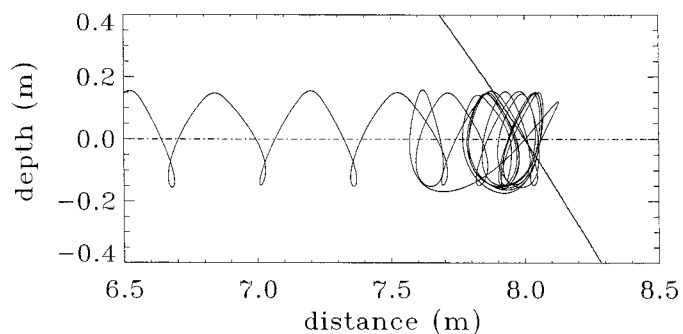


Fig. 11. A side view of the path followed by an idealized kelp frond as it is released from an arbitrary depth into a wave field plus a current that is moving from left to right. The still-water surface is shown as a dotted horizontal line, and a radius showing the extent of the untensioned stipe is indicated on the right-hand side.

relative motion can drop to zero but only for short periods. Furthermore, while not directly comparable instantaneously, $|\bar{u}_w + u_c|$ and $|\bar{u}_r|$ are of similar magnitude in a wave-averaged sense after removing the mean velocity. Contrary to the float simulation (Fig. 9a), the three time series are in phase.

Discussion

The addition of a current and appropriate drag coefficient to the model of UD96 has provided a new model that well simulates our remotely sensed in situ measurements of the motion of a kelp proxy (tethered float) in waves. Application of the model to a subtidal kelp frond, using drag forces appropriate to the low velocities they encounter, has provided interesting new information on kelp frond behavior in waves and currents. In the following section, we use sensitivity analysis to explore which of the model parameters are likely to be most important in determining how kelps react to the forces imparted by waves.

A sensitivity analysis—In this sensitivity analysis, the model parameters considered most likely to exert influence on the response of the kelp to waves are varied one at a time, where possible, using parameter values that are well described in the literature. Our model contains four major environmental parameters (wave height H , wave period T , current velocity u_c , and water depth d), four major frond

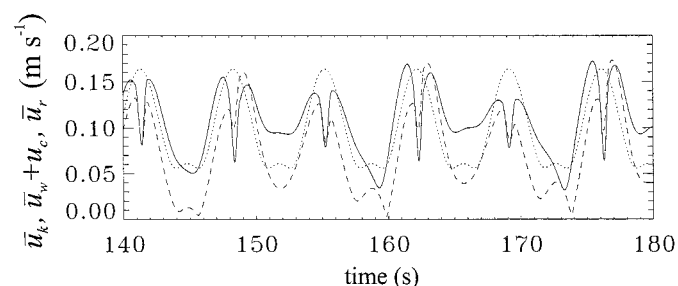


Fig. 12. Kelp frond model results of velocity magnitudes showing $|\bar{u}_k|$ (solid), $|\bar{u}_w + \bar{u}_c|$ (dotted), and $|\bar{u}_r|$ (dashed).

properties (buoyancy B , surface area A , volume V , and stipe length l_0), and three major biomechanical coefficients (drag coefficient C_d , acceleration coefficient C_a , and tension coefficient C_t). Quantifying the response of \bar{u}_r throughout this multidimensional space is essentially boundless. Fortunately, it is possible to limit the ranges of each parameter and consider only those parameters that have significant interest or impact on the model. The environmental parameters are well described in the literature (e.g., Jackson 1998), and the ranges are relatively limited in their variation. The frond properties listed above are not well known, with the exception of l_0 , despite the wealth of published data for *Macrocystis*. Also, studies of *Macrocystis* indicate substantial natural variability in frond properties (e.g., Druehl and Kemp 1982), which should be taken into account in future modeling. For kelp biomechanical parameters, while the responses of kelps to breaking waves in intertidal regions are relatively well documented (e.g., Gaylord et al. 1994; Gaylord 2000), our measurements revealed nearly an order of magnitude increase in C_d under slow compared to fast currents, illustrating a need for further testing of these coefficients at low flow rates. We suggest that a better understanding of these various properties is required before the absolute reliability of modeling can be examined in greater detail.

The relative effects of varying model parameters were compared using Δu defined as the root mean square (RMS) of the magnitude of \bar{u}_r , in excess of u_c for values of u_c ranging from 0.05 to 0.5 m s^{-1} . Figure 13 shows $\Delta u = \text{RMS}(|\bar{u}_r|) - u_c$ as a function of u_c . Each panel plots the standard run using the variable u_c , with all other parameters described in the previous section. In addition, a set of runs with a single variable magnified and reduced is superposed as dotted and dashed lines on each panel. The standard run indicates a slightly decreasing Δu , from ~ 0.06 to 0.025 m s^{-1} . These values are small but substantially larger than the u_c , at least for smaller u_c . The Δu passes through a minimum at $\sim 0.1 \text{ m s}^{-1}$ and then increases with a further increase in u_c . This coincided with the tension being applied every wave period, instead of less frequently, as seen in Fig. 3. The large Δu at low u_c is especially relevant to diffusion boundary layers because it implies that low background water motion might still result in significant boundary layers.

Although the C_d is already a function of u_c , if it is systematically reduced by a factor of 10 in addition to the velocity functionality, then the dashed line of Fig. 13a results—representing nearly a 50% increase over most of the u_c range. This variation allows examination of Δu using the equivalent C_d to the UD96 high-speed S_d . The Δu is substantially larger because the kelp frond does not experience the local velocity. The greater variability is because the frond keeps trying to cross the water surface, which has been shown to generate a highly variable response. Increasing the drag coefficient by a factor of 10 reduced the relative motion as it directly enhanced the force opposing the flow in the \bar{u}_r direction. Above $u_c = 0.3 \text{ m s}^{-1}$, the Δu increases because the drag overcomes buoyancy, and the kelp is pulled beneath the surface. Note that this sensitivity analysis found a number of instances when the frond would be suspended at some intermediate depth balancing drag and buoyancy. However, in most experiments, once the frond was pulled beneath the

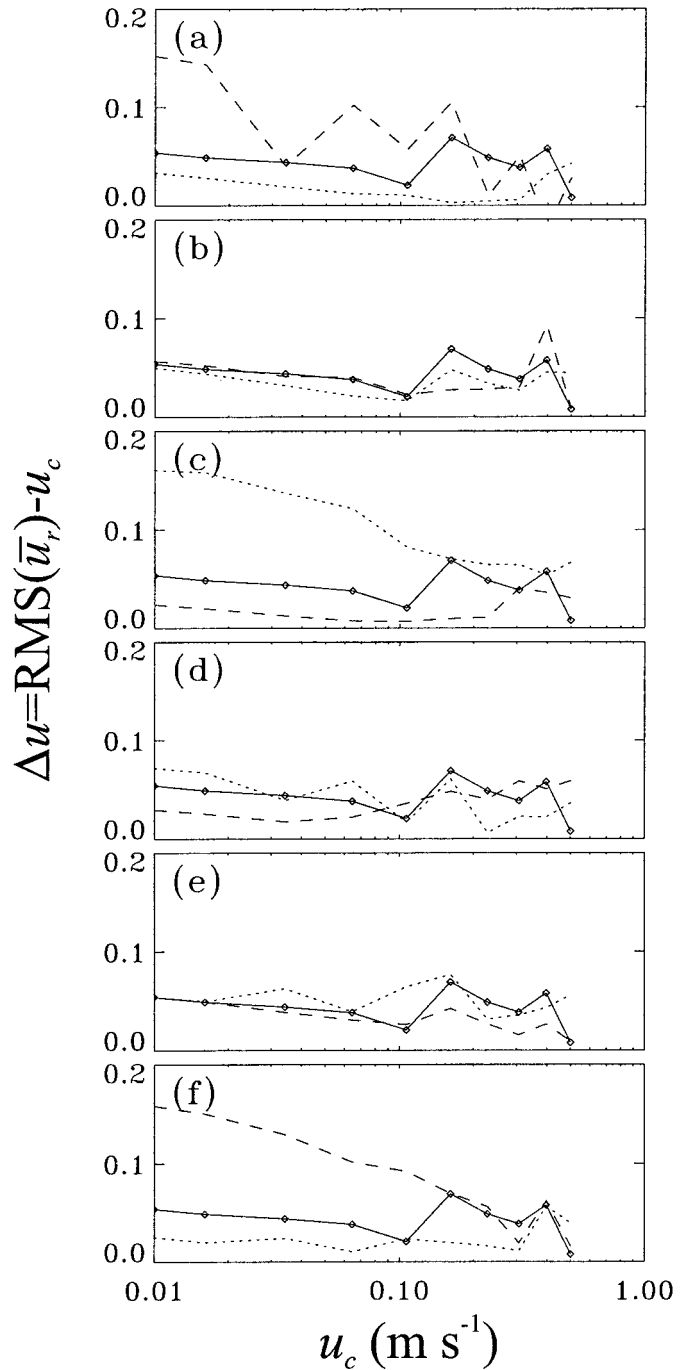


Fig. 13. Results of a sensitivity analysis of the model quantified using Δu (see text). The standard run (solid line) is included in each graph, along with the effect of increasing (dotted line) or decreasing (dashed line) each given parameter. Each line is formed by 10 simulations at values of u_c between 0.0 and 0.5 m s^{-1} as indicated by the symbols on the solid line. The parameters varied were (a) the drag coefficient: $0.1C_d$ and $10C_d$; (b) stipe length: $0.5l_0$ and $2l_0$; (c) wave height: $0.5H$ and $2H$; (d) acceleration coefficient: $0.1C_a$ and $10C_a$; (e) tension coefficient: $0.1C_t$ and $10C_t$; and (f) wave period: $0.5T$ and $2T$.

surface, it tended to keep moving downwards until it lay flat on the bed. This modeled behavior of kelp fronds occurs naturally, as *M. pyrifera* have been observed to lie flat against the bed in strong currents (Kain 1982). The bed boundary condition was set to limit vertical motion.

The short stipe (Fig. 13b, dotted) appeared to reduce the increased Δu of the standard run above $u_c = 0.2 \text{ m s}^{-1}$, and the last three points ($u_c > 0.3 \text{ m s}^{-1}$) are from the frond being held beneath the surface. This reduced stipe length is equal to the still-water depth. Increasing the stipe length also acted to retard the increased Δu above 0.1 m s^{-1} . At this stage, it is not clear why the standard modeling has found local minima in Δu with respect to the stipe length, but possibly it is related to a change in behavior, as the short stipe is equal to the still-water depth.

Increasing the wave height has a substantial effect on Δu at low velocities (Fig. 13c). This occurs because the wave height directly controls the “distance” the frond travels in any wave period. The increase in Δu for the half-H simulations (dashed) occurs at the larger u_c , but the frond is still at the surface.

Figure 3 indicates the importance of C_a . However, this does not appear to be strongly sensitive to the magnitude of C_a (Fig. 13d). Reducing C_a has a similar magnitude of effect to increasing C_d . Perhaps, as its effect is often transient, an averaged quantity like Δu does not fully elucidate its significance in situations where transients play a large role in boundary-layer renewal (Stevens and Hurd 1997). Also, C_a is dependent on the boundary condition at the surface (Fig. 3), which is based on intuition rather than direct observation. While Gaylord et al. (1994) considered acceleration in mainly short-stiped intertidal morphologies, the significant effect of the accelerative force here suggests that further work is required on C_a for long-stiped species such as *Macrocystis* and *Nereocystis*.

We initially thought that the effect whereby the elastic kelp stipe rapidly pulled the kelp frond through the wave crest might be dominant in enhancing Δu . This is possible at low drag coefficients. However, in the present C_d range, it is clear that the F_d and F_a quickly retard any substantial elastic snapping of the frond. Furthermore, even when the low drag coefficient was used, this enhanced the modulation already seen where it would take more than one wave period for the frond to pull its tether tight (with a low drag coefficient and a large C_r , it was possible to force the kelp frond against the current and upstream of the holdfast). This is consistent with the observation of period doubling observed by Denny et al. (1997) and suggests that the magnitude of the current is important in determining the occurrence of this effect. The multiple paths traced by the frond (Fig. 11) can be interpreted as the onset of chaotic motion, especially if one were to consider driving the motion with a continuous wave spectrum.

Improvements in parameterization—While we have determined that higher C_d values were required for sensible modeling at lower speeds, a number of the other model parameters need further consideration. Questions remain about the wetted area when the blades are floating flat on the water surface. Potentially, only half the blade is sustaining any

stress imparted by the flows. While improvements in certainty to within a factor of 2 is of marginal significance compared to the uncertainties and natural variations in other model parameters, determination of A is integral to the correct usage of C_d (Denny 1988). For instance, the orientation of blades along the stipe will influence the value of C_d , which must result in a varying drag force throughout a wave cycle. However, the large velocities at the wave crest last for only a brief instant, so it is possible that the frond shape cannot adjust rapidly enough for steady-state parameterization to be valid.

In addition, we have not incorporated breaking waves into our modeling. A frond at the surface that encounters a breaking wave plume will be subjected to enhanced velocities as the plume moves at a speed approaching the phase speed of the wave. This was beyond the scope of the present work, although clearly with the HH-mode radar, there is great potential for determination of the direct response to the break wave.

We identified frond buoyancy as being of great importance, but there is even less description for this parameter in the literature than for C_d . In our experiments, ρ_k appeared to be comparable with that inferred from UD96, yet if the value was any greater (i.e., less buoyant), the frond buoyancy was unable to hold the frond at the surface even in what was only a moderate current (0.2 m s^{-1}).

The present work considers only the flow in the direction of the waves. It is clear from many observations that waves and currents will not be co-linear (Seymour et al. 1989; Elwany et al. 1995). It is beyond the scope of the present work to quantify this, except to ask whether one should simplify the problem by working in either the plane aligned with the current or the waves (as in the present study). It appears that each facet is equally important. The sensitivity analysis showed that the wave properties strongly affected the results while all results were clearly linked to u_c . This suggests that a three-dimensional approach is required.

The successful application of the dual-polarized microwave radar suggests an encouraging avenue for further work on kelp species with surface-floating canopies. We have performed some additional radar work looking at reflections from the canopy structure itself, but this work is in its infancy.

Conclusions

This study of a fundamental property in algal hydrodynamics and biomechanics, \bar{u}_r , illustrates how modeling in conjunction with experimental observation yields insight into kelp frond dynamics. Remote-sensing observation of tethered floats provides a novel way of testing a model that is then applied to a kelp frond. The potential to examine the kelp response against a range of parameters is apparent. The following points may be concluded.

(1) Low-speed ($<0.5 \text{ m s}^{-1}$) drag coefficients are clearly larger than those obtained by using velocity-adjusted shape factors derived from measurements at greater ambient speeds. The added mass coefficient is important near the water surface, but present understanding of frond behavior

at the water surface is very limited. Furthermore, the interaction at the surface and the drag-induced submersion of the frond requires knowledge of the kelp density, which is poorly documented.

(2) Measurement of unidirectional currents, as well as waves, is important for the correct understanding of kelp frond behavior. In the simplest sense, the current can significantly affect the response at frequencies lower than the wave frequency.

(3) The relative velocity \bar{u}_r cannot be ignored and may be at least as large as velocities measured in the frame of reference of the kelp bed. It is especially influenced by wave parameters such as wave height and period. The relative velocity is strongly related to the wave properties as well as to the current and the drag coefficient.

(4) There is a need for further instrumentation development to derive in situ velocity measurements. Meanwhile, this work illustrates that remote-sensing devices like microwave radar are powerful tools for resolving motion of objects at the water surface.

References

- DEAN, R. G., AND R. A. DALRYMPLE. 1984. Water wave mechanics for engineers and scientists. Prentice.
- DENNY, M. W. 1988. Biology and the mechanics of the wave-swept environment. Princeton Univ. Press.
- , B. P. GAYLORD, AND E. A. COWEN. 1997. Flow and flexibility. II. The roles of size and shape in determining wave forces on the bull kelp *Nereocystis luetkeana*. *J. Exp. Biol.* **200**: 3165–3183.
- , ———, B. HELMUTH, AND T. DANIEL. 1998. The menace of momentum: Dynamic forces of flexible organisms. *Limnol. Oceanogr.* **43**: 955–968.
- DRUEHL, L. D., AND L. KEMP. 1982. Morphological and growth responses of geographically isolated *Macrocystis integrifolia* populations when grown in a common environment. *Can. J. Bot.* **60**: 1409–1413.
- ELWANY, M. H. S., W. C. O'RIELLY, R. T. GUZA, AND R. T. FLICK. 1995. Effects of southern California kelp beds on waves. *J. Waterway Port Coastal Ocean Eng.* **121**: 143–150.
- GAYLORD, B. 2000. Biological implications of surf-zone flow complexity. *Limnol. Oceanogr.* **45**: 174–188.
- , C. BLANCHETTE, AND M. W. DENNY. 1994. Mechanical consequences of size in wave-swept algae. *Ecol. Monogr.* **64**: 287–313.
- HAY, C. H. 1990. The distribution of *Macrocystis* (Phaeophyta: Laminariales) as a biological indicator of cool sea surface temperature, with special reference to New Zealand waters. *J. R. Soc. NZ* **20**: 313–336.
- HURD, C. L. 2000. Water motion, marine macroalgal physiology, and production. *J. Phycol.* **36**: 453–472.
- , P. J. HARRISON, AND L. D. DRUEHL. 1996. Effect of sea water velocity on inorganic nitrogen uptake by morphologically distinct forms of *Macrocystis integrifolia* from wave-sheltered and exposed sites. *Mar. Biol.* **126**: 205–214.
- , AND C. L. STEVENS. 1997. Flow visualization around single and multiple-bladed seaweeds with varying morphologies. *J. Phycol.* **33**: 360–367.
- JACKSON, G. A. 1998. Currents in the high drag environment of a coastal kelp stand off California. *Cont. Shelf Res.* **17**: 1913–1928.
- , AND C. D. WINANT. 1983. Effect of a kelp forest on coastal currents. *Cont. Shelf Res.* **2**: 75–80.
- KAIN, J. M. 1982. Morphology and growth of the giant kelp *Macrocystis pyrifera* in New Zealand and California. *Mar. Biol.* **67**: 143–157.
- KOEHL, M. A. R., AND R. S. ALBERTE. 1988. Flow, flapping, and photosynthesis of *Nereocystis luetkeana*: A functional comparison of undulate and flat blade morphologies. *Mar. Biol.* **99**: 435–444.
- LOBBAN, C. S. 1978. The growth and death of the *Macrocystis* sporophyte (Phaeophyceae, Laminariales). *Phycologia* **17**: 196–212.
- MÉNDEZ, F. J., I. J. LOSADA, AND M. A. LOSADA. 1999. Hydrodynamics induced by wind waves in a vegetation field. *J. Geophys. Res. Oceans* **104**: 18383–18396.
- MUSCHENHEIM, D. K., J. GRANT, AND E. L. MILLS. 1986. Flumes for benthic ecologists: Theory, construction and practice. *Mar. Ecol. Prog. Ser.* **28**: 185–196.
- POULTER, E. M., M. J. SMITH, AND J. A. MCGREGOR. 1995. S-band FMCW radar measurements of ocean surface dynamics. *J. Atmos. Ocean. Technol.* **12**: 1271–1286.
- REES, W. G. 1990. Physical principals of remote sensing. Cambridge Univ. Press.
- SEYMOUR, R. J. 1996. Discussion of effects of southern California kelp beds on waves. *J. Waterway Port Coastal Ocean Eng.* **122**: 207–208.
- , M. J. TEGNER, P. K. DAYTON, AND P. E. PARNELL. 1989. Storm wave induced mortality of giant kelp, *Macrocystis pyrifera*, in Southern California. *Estuarine Coastal Shelf Sci.* **28**: 277–292.
- SMITH, M. J., E. M. POULTER, AND J. A. MCGREGOR. 1996. Doppler radar measurements of wave groups and breaking waves. *J. Geophys. Res.* **101**: 14269–14282.
- STEVENS, C. L., AND C. L. HURD. 1997. Boundary-layers around aquatic macrophytes. *Hydrobiologia* **346**: 119–128.
- , E. M. POULTER, M. J. SMITH, AND J. A. MCGREGOR. 1999. Non-linear features in wave-resolving radar observations of ocean waves. *IEEE J. Ocean. Eng.* **24**: 470–480.
- UTTER, B. D., AND M. W. DENNY. 1996. Wave-induced forces on the giant kelp *Macrocystis pyrifera* (Agardh): Field test of a computational model. *J. Exp. Biol.* **199**: 2645–2654.

Received: 8 October 1999

Accepted: 10 November 2000

Amended: 13 December 2000